Geophys. J. Int. (2008) **172,** 651–662 doi: 10.1111/j.1365-246X.2007.03652.x

Scaling relations of earthquakes and aseismic deformation in a damage rheology model

Vladimir Lyakhovsky[1] and Yehuda Ben-Zion[2]

[1] *Geological Survey of Israel, Jerusalem* 95501, *Israel. E-mail: vladi@geos.gsi.gov.il*
[2] *Department of Earth Sciences, University of Southern California Los Angeles,* CA 90089-0740*, USA*

Accepted 2007 October 8. Received 2007 October 8; in original form 2007 February 27

SUMMARY

We perform analytical and numerical studies of scaling relations of earthquakes and partition of elastic strain energy between seismic and aseismic components using a thermodynamically based continuum damage model. Brittle instabilities occur in the model at critical damage level associated with loss of convexity of the strain energy function. A new procedure is developed for calculating stress drop and plastic strain in regions sustaining brittle instabilities. The formulation connects the damage rheology parameters with dynamic friction of simpler frameworks, and the plastic strain accumulation is governed by a procedure that is equivalent to Drucker–Prager plasticity. The numerical simulations use variable boundary forces proportional to the slip-deficit between the assumed far field plate motion and displacement of the boundary nodes. These boundary conditions account for the evolution of elastic properties and plastic strain in the model region. 3-D simulations of earthquakes in a model with a large strike-slip fault produce scaling relations between the scalar seismic potency, rupture area, and stress drop values that are in good agreement with observations and other theoretical studies. The area and potency of the simulated earthquakes generally follow a linear log–log relation with a slope of 2/3, and are associated with stress drop values between 1 and 10 MPa. A parameter-space study shows that the area-potency scaling is shifted to higher stress drops in simulations with parameters corresponding to lower dynamic friction, more efficient healing, and higher degree of seismic coupling.

Key words: Creep and deformation; Elasticity and anelasticity; Earthquake dynamics; Dynamics and mechanics of faulting; Rheology and friction of fault zones.

1 INTRODUCTION

The brittle portion of the Earth lithosphere is 'damaged' in the sense that any macroscopic rock volume in that layer contains an internal distribution of joints and faults. These fractures have in general complex geometries with intersections, stopovers, bends and many other deviations from planarity. The material around such geometrical complexities is subjected to large stress concentrations, which necessarily lead during continuing deformation to the evolution of the elastic properties and geometry of the actively deforming regions. The evolving material and geometrical properties should be taken into account in quantitative analysis of earthquakes in large spatio-temporal domains, containing several moderate and large faults and earthquake cycles. Building on earlier works, Lyakhovsky *et al*. (1997a, 2001a), Ben-Zion *et al*. (1999), Ben-Zion & Lyakhovsky (2002, 2006) and Hamiel *et al*. (2004) developed a thermodynamically based continuum damage rheology framework for coupled evolution of earthquakes and faults, and used it to study various aspects of seismicity patterns including properties of large earthquake cycles, frequency-size statistics, accelerated seismic release and aftershocks.

Our previous studies of seismicity patterns with the damage rheology model adopted the simplifying assumption that during brittle instability the local deviatoric stress drops to zero. In terms of frictional frameworks, this assumption corresponds to a zero value of the dynamic friction. In this work, we generalize the damage model to include during brittle instability a drop of the local deviatoric stress to a finite value corresponding to non-zero dynamic friction. The plastic strain in zones sustaining brittle instability is computed with a procedure that is mathematically equivalent to the Drucker–Prager plasticity model (Drucker & Prager 1952). We also generalize the boundary conditions to account for the evolution during simulations of elastic properties in the region under consideration. Calculations with the generalized model produce, for ranges of parameters, scaling relations between seismic potency, failure area and stress drop that are compatible with seismological observations. The partitions between seismic and aseismic deformation in various 3-D simulations agree generally with the analytical results of Ben-Zion & Lyakhovsky (2006).

In the next section we review the main aspects of the damage rheology model and provide a background for this work. In Section 3, we present a new mathematical procedure for calculating

irreversible strain accumulation during brittle instabilities. In Section 4, we discuss the set-up of the 3-D numerical model and the general boundary conditions. Results based on the numerical simulations are presented in Sections 5 and 6. A discussion of the results in relation to earthquake quantities and evolution of fault zone structures is given in Section 7.

2 A VISCOELASTIC DAMAGE RHEOLOGY MODEL

The damage rheology we use (Lyakhovsky & Myasnikov 1984, 1985; Lyakhovsky *et al*. 1997a,b; Hamiel *et al*. 2004; Ben-Zion & Lyakhovsky 2006) accounts for the following three general aspects of brittle rock deformation:

1. *Mechanical aspects*. The effective elastic moduli of a cracked solid depend on a scalar variable, termed material damage, representing the local microcrack density.
2. *Kinetic aspects.* The damage evolves as a function of the ongoing deformation, leading to degradation and recovery of the effective elastic moduli and accumulation of inelastic strain beyond the purely elastic regime.
3. *Dynamical aspects*. Macroscopic instability at a critical level of damage.

The theoretical developments of the damage rheology are done within a framework of continuum mechanics and irreversible thermodynamics (e.g. Onsager 1931; Prigogine 1955; deGroot & Mazur 1962; Sedov 1968; Malvern 1969; Ziegler 1983; Kachanov 1986; Rabotnov 1988). The results are applicable to volumes with a sufficiently large number of cracks that allow quantitative description through properties of the crack distribution rather than those of the individual cracks. Discrete models of damage associated with fibre bundles or other discrete elements can lead to similar results in the limit of a large number of elements (e.g. Krajcinovic 1996; Newman & Phoenix 2001; Shcherbakov & Turcotte 2003; Turcotte *et al.* 2003). The thermodynamically based two-phase model for compaction and damage of Bercovici *et al.* (2001), Ricard & Bercovici (2003) and Bercovici & Ricard (2003) accounts for viscous rock deformation but leaves out elasticity. That model was successfully applied to study shear localization and plate boundary formation, but is not appropriate for analysis of brittle failures in the seismogenic zone where elastic deformation plays the dominant role. Ben-Zion *et al*. (1999), Lyakhovsky *et al.* (2001a) and Ben-Zion & Lyakhovsky (2002) used the 2-D thin-sheet approximation to develop a self-consistent physical framework for calculating the simultaneous evolution of earthquakes, fault structures and associated deformation fields in a seismogenic crust governed by damage rheology of Lyakhovsky *et al*. (1977a,b). The framework was extended by Ben-Zion & Lyakhovsky (2006) to a fully 3-D structure consisting of a brittle upper crust governed by damage rheology and ductile viscoelastic substrate. In the following sections we provide additional developments to the 3-D model and use the improved framework to study basic scaling relations of earthquakes.

Lyakhovsky *et al*. (1997b) modelled the mechanical effects of an existing crack population (damage) by generalizing the elastic strain energy function of a deforming solid to the form

$$U = \frac{1}{\rho}\left(\frac{\lambda}{2}I_1^2 + \mu I_2 - \gamma I_1\sqrt{I_2}\right), \tag{1}$$

where $I_1 = \varepsilon_{kk}$ and $I_2 = \varepsilon_{ij}\varepsilon_{ij}$ are the first and second invariants of the elastic strain tensor ε_{ij}, λ and μ are the Lamé parameters of linear Hookean elasticity, and γ is a third modulus for a damaged solid. The result was obtained using the self-consistent formulation of Budiansky & O'Connell (1976) for non-interacting cracks that dilate and contract in response to tension and compression. The obtained potential form is the simplest mathematical expression (e.g. Ben-Zion & Lyakhovsky 2006) for the elastic strain energy that generalizes the classical potential to a non-analytical second-order function of two strain invariants I_1 and I_2. Changes in the effective elastic moduli under stress reversal in a four-point beam test (Weinberger *et al*. 1994), rock dilation due to deviatoric stresses (Hamiel *et al*. 2005) and other rock mechanics experiments (Lyakhovsky *et al*. 1993, 1997b) confirm the applicability of the non-linear stress–strain relations derived from the potential (1).

The kinetic aspects of the damage rheology model are accounted for by making the moduli λ, μ and γ functions of an evolving damage state variable $0 \leq \alpha \leq 1$. Agnon & Lyakhovsky (1995) assumed for simplicity that the moduli μ and γ are linear functions of α and the modulus λ is constant. Later analysis of laboratory acoustic emission and stress–strain data (Hamiel *et al*. 2004) showed that the quality of data fitting may be improved assuming a power law relation between α and the elastic moduli. Hamiel *et al*. (2004, 2006) demonstrated that the model with a power-law accounts for a transition from stable to unstable fracturing, strength evolution and the Kaizer effect. However, assuming constant λ and using linear relations of μ and γ to α still provides a good approximation for conditions of the seismogenic zone.

Using the balance equations of energy and entropy, the entropy production density is represented as a product of a thermodynamic flux ($\mathrm{d}\alpha/\mathrm{d}t$) and a thermodynamic force ($\partial U/\partial\alpha$). Onsager (1931) theoretically generalized empirical laws established by Fourier, Ohm, Fick and Navier, and proposed linear relations between thermodynamic forces and fluxes (see review by Martyushev & Seleznev 2006). For small deviations from equilibrium, the Onzager principle can be obtained from the maximum entropy production principle, or maximum dissipation rate of mechanical energy, or the Mises principle (e.g. Ziegler 1983; Martyushev & Seleznev 2006). Adopting the Onsager principle, our equation of damage evolution has the form (Lyakhovsky *et al*. 1997a)

$$\frac{\mathrm{d}\alpha}{\mathrm{d}t} = -C\frac{\partial U}{\partial \alpha}, \tag{2}$$

where the positive kinetic function of state variables C leads to a non-negative local entropy production related to damage evolution during both material degradation and recovery. The transition from damage accumulation to healing is controlled by the value of the strain invariant ratio $\xi = I_1/\sqrt{I_2}$, which appears often in the equations of our damage model. The value $\xi = \xi_0$ controls the transition from healing to damage accumulation. Lyakhovsky *et al*. (1997a) related the ξ_0 value to the internal friction of intact rock, and estimated $\xi_0 = -0.8$ for rock with internal friction $f = 0.6$ and Poisson ratio $\nu = 0.25$. Lyakhovsky *et al*. (1997a) suggested that $C = C_\mathrm{d}/\gamma_\mathrm{m}$ is a material constant for damage increase (degradation) at $\xi > \xi_0$, where γ_m is the maximum value of the third modulus in (1) discussed further below. They estimated the C_d value to vary from 0.5 to 5 s^{-1} for different rocks tested at relatively high confining pressures and room temperature. However, Lyakhovsky *et al*. (2005) showed that the damage model with a constant C significantly overestimates the strength of Westerly granite at low confining pressures. They suggested a pressure-dependent relation that varies exponentially with a characteristic scale of 50 MPa, indicating that for simulations of fracture processes at depth larger than about 3–5 km, C_d may be taken as a constant.

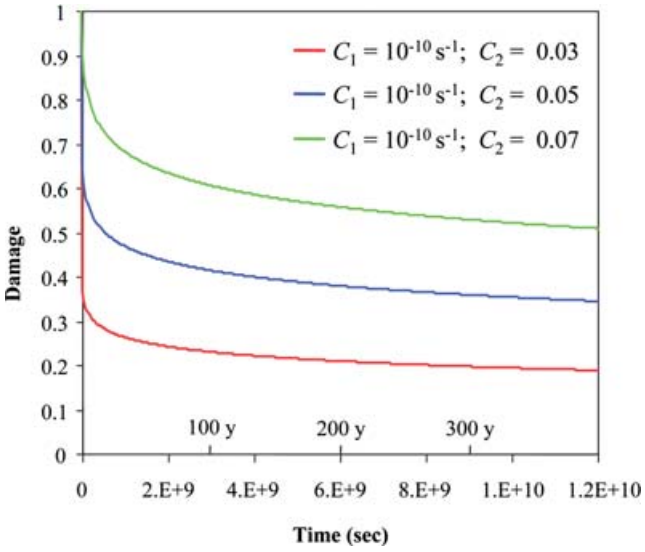

Figure 1. Damage decrease (healing) for different values of the healing parameter C_2 and 200 MPa lithostatic pressure.

The recovery of elastic moduli at $\xi < \xi_0$ is associated with healing of microcracks and is favoured by high confining pressure, low shear stress and high temperature. Motivated by the observed logarithmic increase (e.g. Dieterich 1978, 1979) of the static coefficient of friction with time, Lyakhovsky *et al*. (1997a) suggested a damage-dependent function for the kinetics of healing of the form $C(\alpha) = C_1 \exp(\alpha/C_2)/\gamma_m$. Lyakhovsky *et al*. (2005) showed that the damage model with the exponential healing in the kinetic eq. (2) reproduces the key observed features of rate- and state-dependent friction, and constrained the damage healing parameters C_1, C_2 based on the laboratory data of Dieterich (1978, 1979) and Linker & Dieterich (1992). They approximated the C_2 value by the ratio $C_2 \sim b/f$ between the parameter b of the friction experiments and the steady-state friction coefficient f. Since $b \sim 1$–5×10^{-2} and $f \sim 0.6$–0.8, the estimated C_2 value falls between 10^{-1} and 10^{-2}. The value of the coefficient C_1 strongly depends on the value of the coefficient C_2, the compaction strain as a result of the imposed loading, and the increase rate of the static coefficient of friction. Hence, the C_1 value is not well constrained and may vary by several orders of magnitude from $C_1 \sim 10^{-12}$ s^{-1} up to 10^{-6} s^{-1}. Fig. 1 shows the expected material healing for $C_1 = 10^{-10}$ s^{-1}, three different values $C_2 = 0.03, 0.05, 0.07$ and 200 MPa lithostatic pressure corresponding to about 7–8 km depth. The material recovery is very fast at the initial stage of healing, but the damage remains relatively high ($\alpha > 0.5$) during hundreds of years for high value of $C_2 = 0.07$. Lower C_2 values lead to more efficient overall healing. During 300 yr the damage decreases to $\alpha = 0.35$ and 0.2 for $C_2 = 0.05$ and 0.03, respectively. Accounting for the form of the kinetic coefficients discussed above, and assuming λ = const. and linear relations between μ, γ and α, the equation for damage evolution (2) becomes

$$\frac{d\alpha}{dt} = \begin{cases} C_d I_2(\xi - \xi_0) & \text{for} \quad \xi > \xi_0 \\ C_1 \exp\left(\dfrac{\alpha}{C_2}\right) I_2(\xi - \xi_0) & \text{for} \quad \xi < \xi_0 \end{cases}. \tag{3}$$

In most of the simulations done in this work (Sections 5 and 6) we use $C_d = 5$ s^{-1}, $C_1 = 10^{-10}$ s^{-1}, and $C_2 = 0.05$. We also illustrate the sensitivity of the model results to more efficient ($C_2 = 0.07$) and less efficient ($C_2 = 0.03$) healing.

As the damage variable α increases, the modulus γ increases from 0 for a damage-free Hookean solid to γ_m ($\alpha = 1$), defined in Section 3 by normalization of the damage variable. The damage increase also leads to decreasing shear modulus μ, increasing Poisson ratio ν, and amplification of the non-linearity of rock elasticity. The process of damage increase becomes unstable with the loss of convexity of the potential (1), leading to macroscopic brittle instability at a critical level of damage. The dynamic stress drop during the brittle instability produces rapid reduction of the elastic strain and increase of plastic deformation that corresponds to slip in simpler models with planar faults. The conditions for loss of convexity and equations describing the process of a macroscopic failure are discussed in the next section.

Comparisons between theoretical predictions and observed deformation and acoustic emission from laboratory experiments in granites and sandstones led Hamiel *et al*. (2004) to incorporate a gradual accumulation of a damage-related irreversible deformation. This gradual inelastic strain, ε^v_{ij}, starts to accumulate with the onset of acoustic emission and the rate of its accumulation is assumed to be proportional to the rate of damage increase:

$$\frac{d\varepsilon^v_{ij}}{dt} = \begin{cases} C_v \dfrac{d\alpha}{dt} \tau_{ij} & \dfrac{d\alpha}{dt} > 0 \\ 0 & \dfrac{d\alpha}{dt} \le 0 \end{cases}, \tag{4}$$

where C_v is a material constant and $\tau_{ij} = \sigma_{ij} - \sigma_{kk}\delta_{ij}/3$ is the deviatoric stress tensor. The compliance or inverse of viscosity ($C_v\, d\alpha/dt$) relates the deviatoric stress to the rate of irreversible strain accumulation. Following Maxwell viscoelastic rheology, the total strain tensor, ε^{tot}_{ij}, is assumed to be a sum of the elastic strain tensor and the irreversible viscous component of deformation, that is, $\varepsilon^{tot}_{ij} = \varepsilon_{ij} + \varepsilon^v_{ij}$. This assumption means that the total irreversible strain accumulated during the loading should be proportional to the overall damage increase in the rock sample. The time scale of the damage-related irreversible strain accumulation is proportional to the time scale of damage accumulation (related to the coefficient C_d of eq. 3) divided by a non-dimensional value $R = \mu_0 \cdot C_v$. Ben-Zion & Lyakhovsky (2006) connected the rate of irreversible strain accumulation with partitioning between seismic and aseismic deformation in the seismogenic zone, and showed that the fraction of elastic strain released seismically, referred to as the seismic coupling coefficient χ, can be estimated as

$$\chi = \frac{1}{1+R}. \tag{5}$$

Analyses of results obtained in rock strength experiments indicate (Hamiel *et al*. 2004, 2006) that granite samples have $R = 0.3$–0.6, corresponding to seismic coupling 60 per cent $< \chi <$ 80 per cent, while Berea sandstone accumulates more irreversible strain and is associated with $R = 1.4$ and $\chi = 42$ per cent.

3 LOSS OF CONVEXITY AND MACROSCOPIC FAILURE

Two mathematically different conditions can be utilized for analysing the macroscopic stability of solid under deformation. The first is convexity of the elastic strain energy, which is necessary for the existence of a unique solution of the static problem (e.g. Ekland & Temam 1976). This criterion was adopted and expanded by Hill, Thomas, Mandel, Trusdell and others in the framework of plasticity theory (e.g. Bazant & Cedolin 1991). The second is a change of the elasto-dynamic equation to ellipticity (e.g. Rudnicki & Rice

Table 1. The Hessian matrix $\partial^2 U/\partial\varepsilon_{ij}\partial\varepsilon_{kl}$.

	ε_{11}	ε_{22}	ε_{33}	ε_{12}	ε_{13}	ε_{23}
ε_{11}	$\lambda+2\mu-\gamma\xi+\gamma\xi e_1^2-2\gamma e_1$	$\lambda-\gamma(e_1+e_2)+\gamma\xi e_1e_2$	$\lambda-\gamma(e_1+e_3)+\gamma\xi e_1e_3$	0	0	0
ε_{22}	$\lambda-\gamma(e_1+e_2)+\gamma\xi e_1e_2$	$\lambda+2\mu-\gamma\xi+\gamma\xi e_2^2-2\gamma e_2$	$\lambda-\gamma(e_2+e_3)+\gamma\xi e_2e_3$	0	0	0
ε_{33}	$\lambda-\gamma(e_1+e_3)+\gamma\xi e_1e_3$	$\lambda-\gamma(e_2+e_3)+\gamma\xi e_2e_3$	$\lambda+2\mu-\gamma\xi+\gamma\xi e_3^2-2\gamma e_3$	0	0	0
ε_{12}	0	0	0	$2\mu-\gamma\xi$	0	0
ε_{13}	0	0	0	0	$2\mu-\gamma\xi$	0
ε_{23}	0	0	0	0	0	$2\mu-\gamma\xi$

Here $e_i=\varepsilon_i/\sqrt{I_2}$ is a normalized value of the deformation along the principal axis 'i'.

1975). These two conditions are not always identical, especially for non-linear elasticity (e.g. Schreyer & Neilsen 1996a,b). The first condition is a stronger one and convexity may be lost prior to the transition to ellipticity, especially in the case of a system constrained by rigid boundary conditions.

In models governed by slip-weakening or rate- and state-dependent friction laws, the occurrence of instability requires that the rate of weakening is larger than the rate of stress reduction (stiffness of the system) on a slipping patch (e.g. Rice 1980; Ben-Zion 2003). Similarly to the loss of convexity, the existence of frictional weakening is a necessary but not a sufficient condition for instability. In detailed frictional models, the transition from aseismic slip to dynamic rupture occurs when the slipping area reaches a critical 'nucleation' size for which the rate of stress reduction is equal to the rate of weakening. In the limit case of static-kinetic friction, adopted in our present treatment of the instability process, the critical nucleation size goes to zero and material weakening becomes a sufficient condition for slip instability. For this reason we use here the condition for convexity loss to indicate the onset of material instability.

The maximum possible value of the damage parameter α for a given strain tensor ε_{ij} is defined by the requirement of convexity of the elastic energy U given by (1). This condition implies positivity of all the eigenvalues of the Hessian matrix ($\partial^2 U/\partial\varepsilon_{ij}\varepsilon_{kl}$), providing a canonical base in the mathematical space of elastic deformations ($\varepsilon_{11},\varepsilon_{22},\varepsilon_{33},\varepsilon_{12},\varepsilon_{13},\varepsilon_{23}$). The Hessian matrix components in the coordinate system of the principal axes are given in Table 1. Lyakhovsky *et al.* (1997a) found two different conditions for positivity of the three eigenvalues of the Hessian matrix in the coordinate system of the principal strain axes. The condition for the first eignvalue is:

$$x_1=2\mu-\gamma\xi=2\mu^e>0, \tag{6}$$

while the condition for the second and third eigenvalues is given by the quadratic equation,

$$x^2-(4\mu-3\gamma\xi+3\lambda)x+(2\mu-\gamma\xi)^2+(2\mu-\gamma\xi)(3\lambda-\gamma\xi)+(\lambda\gamma\xi-\gamma^2)(3-\xi^2)=0.$$

The roots of this equation are positive if

$$(2\mu-\gamma\xi)^2+(2\mu-\gamma\xi)(3\lambda-\gamma\xi)+(\lambda\gamma\xi-\gamma^2)(3-\xi^2)>0. \tag{7}$$

Fig. 2 shows the dependence of the critical damage on the strain invariant ratio ($\xi=I_1/\sqrt{I_2}$) for $\lambda_0=\mu_0$. The condition (7) is realized first for $\xi\geq\xi_0$ and prescribes a scale for $\gamma_{\rm m}$, denoting the maximum value of γ, using $\xi=\xi_0$ and $\alpha=1$. The condition (6) implies the vanishing of the effective shear modulus and is realized for relatively high positive values of ξ typical for tensile stresses. For characteristic depths of a seismogenic zone, the positive damage evolution (damage accumulation path in Fig. 2), which starts at

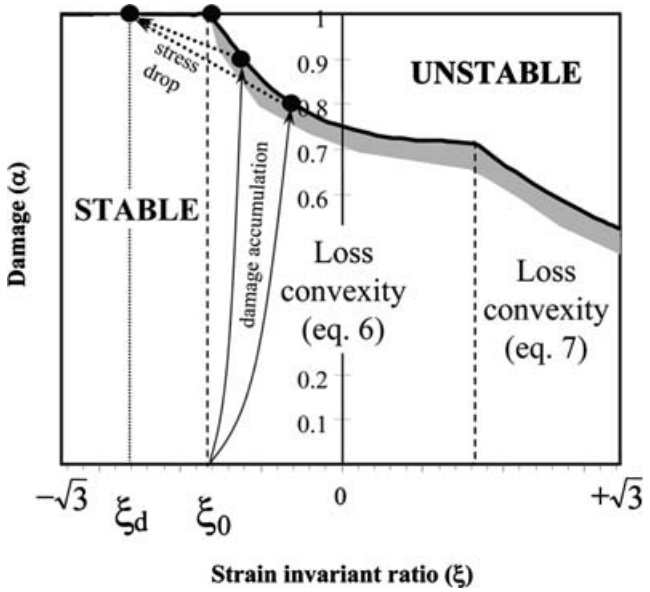

Figure 2. A schematic diagram illustrating the evolution of damage versus the strain invariant ratio ($\xi=I_1/\sqrt{I}$) for $\lambda_0=\mu_0$. The damage parameters ξ_0 and $\xi_{\rm d}$ correspond to static and dynamic friction values in simpler frictional frameworks. See text for additional details.

$\xi=\xi_0$, is expected to meet first the condition (7) corresponding to frictional sliding on a surface. The grey region denotes schematically a correction for the reduction of the critical level of damage for the propagation of rupture instability by a dynamic weakening factor (Ben-Zion & Lyakhovsky 2006).

To understand the physical meaning of condition (7) it is useful to examine the constitutive stress–strain relations for the stress tensor σ_{ij}, obtained by differentiation of the elastic energy (1):

$$\sigma_{ij}=\rho\frac{\partial U}{\partial\varepsilon_{ij}}=\left(\lambda-\frac{\gamma}{\xi}\right)I_1\delta_{ij}+(2\mu-\gamma\xi)\,\varepsilon_{ij}. \tag{8}$$

Using the stress–strain relation (8), Lyakhovsky *et al*. (1993) connected the stress invariant ratio $J_1/\sqrt{J_2}$ with the strain invariant ratio:

$$\frac{J_1}{\sqrt{J_2}}=f(\alpha,\xi)=\frac{(3\lambda+2\mu)\,\xi-3\gamma-\gamma\xi^2}{(2\mu-\gamma\xi)\sqrt{1-\xi^2/3}}, \tag{9}$$

where the three elastic moduli λ, μ, γ are functions of the damage variable α, and the invariants J_1 and J_2 of the stress tensor are:

$$J_1=\sigma_{ij}\delta_{ij},$$

$$J_2=\left(\sigma_{ij}-\frac{1}{3}J_1\delta_{ij}\right)\left(\sigma_{ij}-\frac{1}{3}J_1\delta_{ij}\right)=\sigma_{ij}\sigma_{ij}-\frac{1}{3}J_1^2.$$

Note that the second strain invariant $\left(I_2=\varepsilon_{ij}\varepsilon_{ij}\right)$ is a product of the elastic strain tensor, while the stress invariant J_2 is a product of

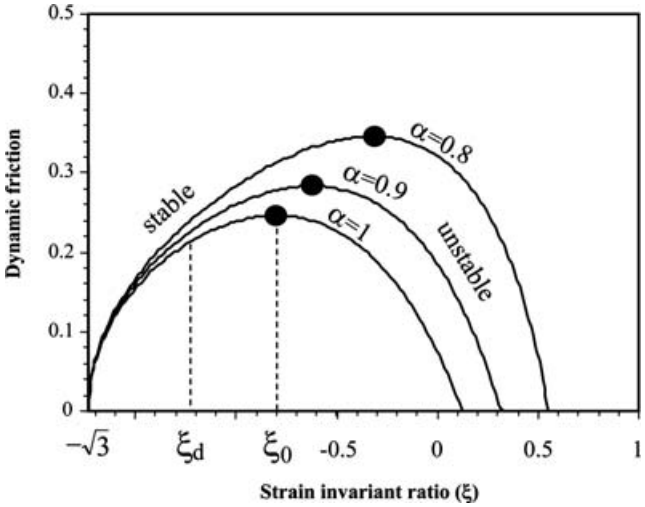

Figure 3. Effective dynamic coefficient of friction after failure versus the strain invariant ratio for values of the damage state variable $\alpha = 0.8, 0.9, 1$.

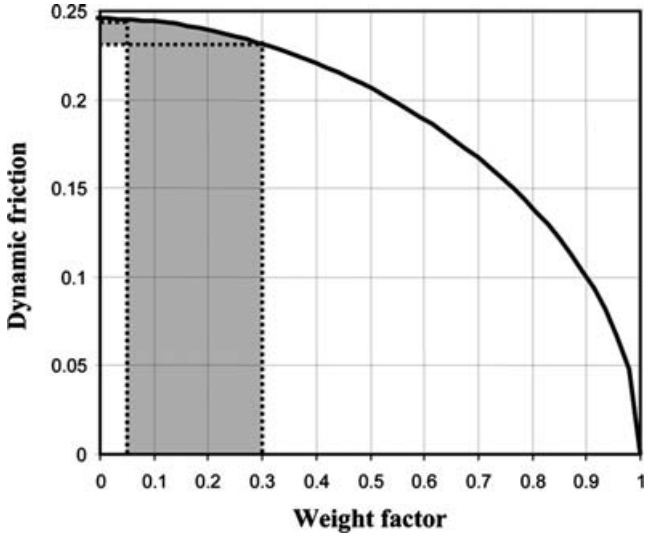

Figure 4. Dynamic coefficient of friction after failure versus the weight factor.

the deviatoric stress tensor. These definitions preserve the traditional notations of the damage rheology and theory of plasticity.

Fig. 3 shows the relation between the effective residual or dynamic coefficient of friction after failure and the strain invariant ratio for several values of the damage parameter $\alpha = 0.8, 0.9, 1$. The conversion from the stress invariant ratio to the effective static coefficient of friction was discussed by Agnon & Lyakhovsky (1995). The maximum value marked on each line corresponds to conditions (6) and (7) of the convexity loss at a given α-value. The cap-shape of the curves in Fig. 3 indicates that the coefficient of friction decreases with increasing shear strain (larger ξ) leading to unstable sliding. This condition is similar to velocity-weakening regime in the rate-state frictional framework (e.g. Ben-Zion 2003). We assume that with the onset of sliding the damage variable increases instantaneously to $\alpha = 1$, and thus the negative slope of the relation between coefficient of friction and ξ leads to dynamic rupture. The dynamic stress drop associated with brittle instability produces a reduction of the elastic strain in a rapid process (not analysed in detail here) and related increase of plastic deformation. The dynamic slip is arrested and post-failure material healing starts when the strain invariant ratio is reduced to a dynamic value ξ_{d} (Figs 2 and 3) corresponding to a stable regime ($-\sqrt{3} \le \xi_{\mathrm{d}} \le \xi_0$).

Similarly to models assuming constant dynamic friction during simulated seismic events (e.g. Ben-Zion & Rice 1993; Ben-Zion 1996; Zöller *et al*. 2006), we define a constant ξ_{d} value using a weight factor, w, as a model parameter:

$$\xi_{\mathrm{d}} = (1 - w) \cdot \xi_0 - w \cdot \sqrt{3}. \tag{10}$$

Fig. 4 illustrates the relation between the dynamic friction and the weight factor for the range $0 < w < 1$. Using eq. (9), the condition for macroscopic stability may be rewritten as a yielding condition relating the stress invariants for a given α and ξ values:

$$Y(\sigma_{ij}) = J_1 - f(\alpha, \xi) \cdot \sqrt{J_2} < 0, \tag{11}$$

where $Y(\sigma_{ij})$ is the yielding function. For positive values of the yielding function $[Y(\sigma_{ij}) \ge 0]$ the system is unstable and plastic strain is accumulated. This mathematical formulation of the problem is equivalent to the classical Drucker–Prager model (Drucker & Prager 1952), which generalizes the classical Coulomb yield condition for a cohesionless material (e.g. Collins & Houlsby 1997; Hill 1998).

According to the Mises principle, the incremental plastic strain tensor, $\mathrm{d}\varepsilon^p_{ij}$, accumulated during plastic flow should provide a maximum dissipation rate of the mechanical energy. This may be achieved by adopting the associated plasticity law of Drucker (1949). The connection between the Drucker's associated plasticity law and the Mises principle was widely discussed in context of thermo-mechanical principles of continua (e.g. Prager 1959; Mosolov & Myasnikov 1965, 1981; Ziegler 1983; Collins & Houlsby 1997; Collins 2005). The associated plasticity law of Drucker (1949) formulated in terms of the incremental stress change, $\mathrm{d}\sigma_{ij}$, implies (e.g. Washizu 1982) that $\mathrm{d}\sigma_{ij}$ is proportional to the gradient $\partial Y/\partial\sigma_{ij}$ of the yielding surface:

$$\mathrm{d}\sigma_{ij} = \mathrm{d}\sigma^e_{ij} - A \frac{\frac{\partial Y}{\partial \sigma_{kl}} d\sigma^e_{kl}}{h + \frac{\partial Y}{\partial \sigma_{pq}} \frac{\partial Y}{\partial \sigma_{pq}}} \frac{\partial Y}{\partial \sigma_{ij}}, \tag{12}$$

where $\mathrm{d}\sigma^e_{ij}$ is incremental elastic stress corresponding to the increment of the total strain $d\varepsilon_{ij}$ through the stress–strain relations (8) and

$$A = \begin{cases} 0, & if \quad Y < 0 \\ 1, & if \quad Y \ge 0 \end{cases}.$$

The relation between the material hardening parameter h of (12) and $\mathrm{d}f$ is derived from the yielding stress condition $\mathrm{d}Y = 0$. Using the derivatives $\partial Y/\partial\sigma_{ij}$:

$$\frac{\partial Y(\sigma_{ij})}{\partial \sigma_{kl}} = \left(1 + \frac{1}{3} f^2\right) \delta_{kl} - f \cdot \frac{\sigma_{kl}}{\sqrt{J_2}} \tag{13}$$

and

$$\frac{\partial Y(\sigma_{ij})}{\partial \sigma_{kl}} \cdot \frac{\partial Y(\sigma_{ij})}{\partial \sigma_{kl}} = 3 + f^2 \tag{14}$$

lead to an equation for the h value

$$h = \mathrm{d}f \cdot \frac{\sqrt{J_2} \cdot \left(3 + f^2\right)}{\mathrm{d}\sigma^e_{ij} \cdot \left[\left(1 + \frac{1}{3} f^2\right) \cdot \delta_{ij} - f \frac{\sigma_{ij}}{\sqrt{J_2}}\right] - \mathrm{d}f \cdot \sqrt{J_2}}. \tag{15}$$

Substituting (13), (14) and (15) back into (12) yields:

$$d\sigma_{ij} = d\sigma^e_{ij} - A\frac{d\sigma^e_{kl}\cdot\left[\left(1+\frac{1}{3}f^2\right)\cdot\delta_{kl} - df\cdot\frac{\sigma_{kl}}{\sqrt{J_2}}\right]}{3+f^2} \cdot\left[\left(1+\frac{1}{3}f^2\right)\cdot\delta_{ij} - f\cdot\frac{\sigma_{ij}}{\sqrt{J_2}}\right]. \quad (16)$$

Eq. 16 describes the local stress drop in a failed element, where one of the conditions for convexity loss (eqs 6 and 7) is met and the damage rheology parameters ξ and α change their values, from those corresponding to the onset of the instability to $\xi = \xi_d$ and $\alpha = 1$ along the path schematically shown in Fig. 2. The overall local stress drop and sensitivity of the scaling relation between the potency of the simulated seismic event and the rupture area is discussed in Section 5.

4 3-D FRAMEWORK FOR NUMERICAL SIMULATIONS

To simulate results relevant to earthquakes and crustal faults, we use the damage rheology in a 3-D regional model (Fig. 5) with three main units of the lithosphere. The upper layer represents a top cover of weak sediments, while the second and third layers represent the crystalline crust and upper mantle, respectively. Ben-Zion & Lyakhovsky (2006) provide a detailed description of the model setup. Here we only outline the main model ingredients.

The total strain tensor ε^t_{ij} in each layer is written as the sum of three strain components associated with different deformation mechanisms

$$\varepsilon^t_{ij} = \varepsilon^e_{ij} + \varepsilon^i_{ij} + \varepsilon^d_{ij}, \quad (17)$$

where ε^e_{ij} is elastic strain related to the stress tensor through (8), ε^i_{ij} denotes the damage-related inelastic strain with accumulation rate calculated using (4), and ε^d_{ij} represents ductile strain. The latter may be generated by a variety of mechanisms including dislocation creep, solid-state diffusion, and solution–diffusion–precipitation processes (e.g. Kohlstedt *et al*. 1995). The ductile strain in the sedimentary layer is governed by Newtonian viscosity with a coefficient $\eta = 10^{22}$ Pa s. The ductile strain in the lower crust and upper mantle are governed by the well-known power-law relation between the shear stress τ and the strain rate $\dot{\varepsilon}$ (e.g. Weertman 1978):

$$\dot{\varepsilon} = A\tau^n \exp\left(-\frac{Q+PV^*}{RT}\right). \quad (18)$$

The parameters A and n are empirical constants, Q is activation energy, V^* is activation volume, P is pressure, T is temperature and R is the gas constant. The material constants $A = 6.31 \times 10^{-20}$ Pa^{-n} s^{-1}, $n = 3.05$ and $Q = 276$ kJ mol^{-1} for a creep law of the diabase (Carter & Tsenn 1987) are used for the ductile flow of the lower crust. These flow parameters may slightly vary according to the composition of the continental crust (e.g. Strehlau & Meissner 1987). Hirth & Kohlstedt (2003) discussed different mechanisms and experimentally based rheological parameters relevant for the ductile flow in the upper mantle. Molnar & Jones (2004) discussed a test for the average viscosity of the mantle lithosphere for a continental region, and suggested that the rheological parameters of wet olivine reported by Hirth & Kohlstedt (1996, 2003) favour flow laws. For relatively low pressures corresponding to depths less than 100 km, the PV^* term in (18) is negligible. The simulations incorporate a depth-dependent temperature gradient of 20 °C km^{-1}, corresponding to a typical heat flow value about 60 mW m^{-2} for the continental lithosphere (e.g. Turcotte & Schubert 2002).

The stress in the model volume under consideration is governed by the lithostatic pressure, mass density, elastic moduli and tectonic loading corresponding to steady plate motion far from the

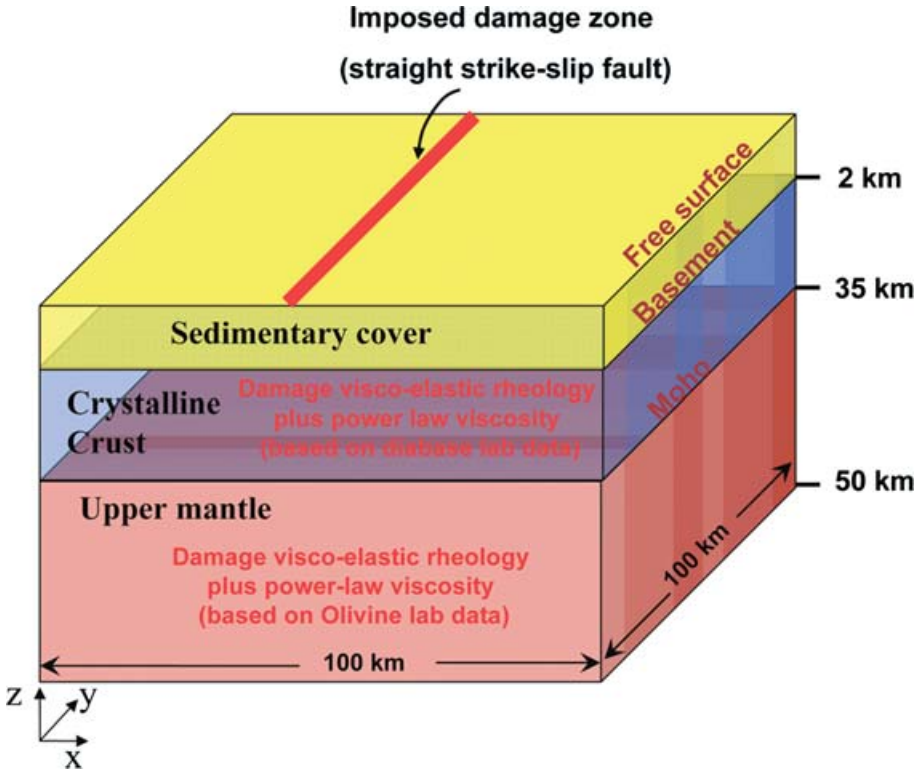

Figure 5. A diagram of the 3-D lithospheric structure used in the numerical simulations.

model region. Numerical modelling of the evolving seismicity and fault patterns in the model region requires specification of appropriate boundary conditions. The condition of constant plate motion at infinity is usually replaced for a finite size model by either constant and uniform fault-parallel velocity, or constant and uniform force. Zeller & Pollard (1992) modelled a single 2-D fracture using both displacement and force boundary conditions. Comparing the numerical and analytical results, they concluded that displacement boundary conditions can introduce significant errors. Lyakhovsky *et al*. (2001a) showed that these seemingly equivalent boundary conditions generate very different velocity and stress distributions during the interseismic period. Ben-Zion & Lyakhovsky (2002) used a constant force condition to analyse the deformation preceding large earthquakes. They obtained a 1-D analytical power-law time-to-failure relation for accelerating seismic release leading to system-size events. These and similar results of Turcotte *et al*. (2003) are consistent with observed seismic activation before some large earthquakes. For the relaxation process in a region following the occurrence of a large event, Ben-Zion & Lyakhovsky (2006) used a constant total strain boundary condition. Simplifying the governing equations, they obtained a 1-D analytical solution for aftershock rates following the modified Omori law. The analytical solutions of Ben-Zion & Lyakhovsky (2002, 2006) were accompanied by 3-D numerical simulations to clarify the conditions for which accelerated seismic release does or does not occur, and factors controlling the aftershocks productivity and rate of aftershocks decay.

The results discussed above indicate that neither constant velocity nor constant force boundary conditions are appropriate for long-term simulations aiming to study the evolution of earthquakes and faults over many large earthquake cycles. The boundary conditions should be updated during simulations to account for the evolution of the elastic properties within a simulated volume, as done with the hybrid FEM/BEM algorithm (e.g. Zienkiewicz *et al*. 1977; Brady & Wassyng 1981; Beer 1983; Beer & Watson 1992; Jing & Hudson 2002) and previous 2-D simulations with the damage model used for analysis of fracture scaling (Lyakhovsky 2001). To perform long-term simulations with appropriate boundary conditions at the edges of a finite-size region, we use variable boundary forces proportional to a stiffness of virtual springs multiplied by the mismatch (slip-deficit) between the far field plate motion and displacement of the boundary nodes (Fig. 6). These boundary conditions are equivalent to a constant force in the limit of very large mismatch between the plate motion and the boundary nodes displacement. In the limit of very large spring stiffness, the applied boundary conditions become equivalent to constant velocity conditions. For intermediate cases, the evolving forces at the boundary nodes model the elastic response of the surrounding rock to the evolution of elastic properties and seismic events within the simulated domain.

The numerical simulations employ the Fast Lagrangian Analysis of Continua (FLAC) algorithm (Cundall & Board 1988; Cundall 1989; Poliakov *et al*. 1993; Ilchev & Lyakhovsky 2001; Lyakhovsky *et al*. 2001b). The simulations are done with tetrahedral elements of variable sizes that increase gradually from about 1 km in the seismogenic zone to about 5 km in the ductile region. Finzi *et al*. (2006) compared the surface deformation associated with a system-size event to analytical solutions and FEM numerical simulations incorporating viscoelastic rheology (e.g. Savage & Prescott 1978; Johnson & Segall 2004). The results validate the use of the 3-D FLAC-based code with the adjustable boundary conditions for fault evolution studies.

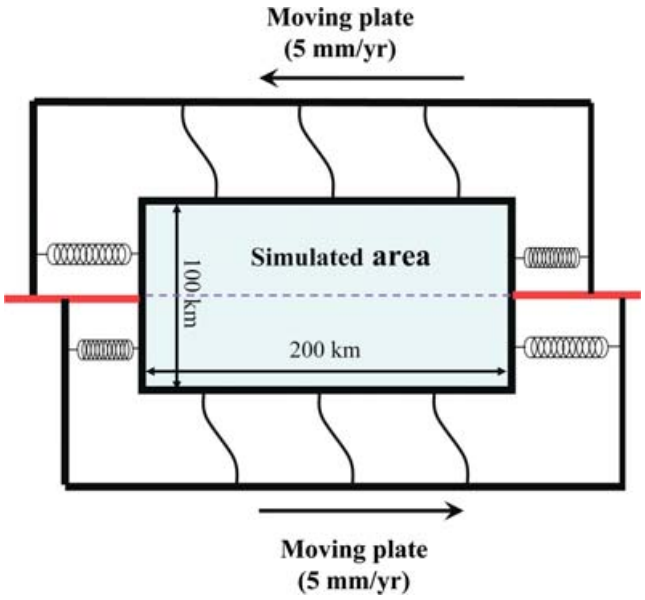

Figure 6. A schematic diagram illustrating the generalized boundary conditions corresponding to a constant plate motion far from the simulated model region.

5 SCALING BETWEEN EARTHQUAKE POTENCY AND RUPTURE AREA

One of the most striking scaling relations for moderate to large earthquakes is the linear relation between the logarithm of rupture area and logarithm of the scalar seismic moment or potency. The seismic potency tensor is defined by the integral (Ben-Zion 2003) of the accumulated plastic strain, ε_{ij}^{p}, over the volume sustaining brittle earthquake deformation

$$P_{ij} = \int_V \varepsilon_{ij}^{p} \mathrm{d}V. \tag{19}$$

The seismic moment tensor is given from the potency tensor by $M_{ij} = \sum c_{ijkl} P_{kl}$, where c_{ijkl} is the tensor of elastic moduli at the source. However, as discussed by Ben-Zion (2001, 2003), and simulated in this paper and our previous related works, the elastic moduli at the source vary rapidly (and are hence ambiguously defined) in the space–time windows associated with earthquakes. In addition, the moduli in the earthquake source regions do not affect the seismic radiation in the surrounding elastic solid and can thus be assigned arbitrarily (e.g. Heaton & Heaton 1989; Ben-Zion 1989; Ampuero & Dahlen 2005). For these reasons we discuss results associated with the seismic potency rather than the more commonly used moment.

Kanamori & Anderson (1975) provided theoretical basis of some empirical relations in seismology and connected the seismic moment with the rupture area and stress drop. Using their results with constant shear modulus (μ) and constant stress drop ($\Delta\sigma$), the relation between the scalar seismic potency (P) and rupture area (S) is expressed as:

$$\log(P) = \frac{3}{2} \cdot \log(S) + \log\left(\frac{16 \cdot \Delta\sigma}{7\pi^{3/2} \cdot \mu}\right). \tag{20}$$

Kanamori & Anderson (1975) analysed the moment-area scaling for interplate earthquakes with surface magnitude $M_S > 5.8$, for which both area and moment are accurately determined, and obtained a good fit for $\Delta\sigma = 3$ MPa. All the data points presented

in their Fig. 2 align well with a small scatter between the lines corresponding to stress drops in the range $\Delta\sigma = 1$–10 MPa. The theoretically predicted linear log–log scaling (20) with a slope of 3/2 was confirmed by analysis of source parameters for strong historical earthquakes (Wells & Coppersmith 1994), as well as synthetic earthquake catalogues in models with planar faults (e.g. Ben-Zion & Rice 1993; Hillers *et al*. 2007). The stress drops of most simulated earthquakes in a planar fault model with heterogeneous rate- and state-dependent friction properties also fall within 1 and 10 MPa (Hillers *et al*. 2007).

The model of Ben-Zion & Rice (1993) for a segmented strike-slip fault zone in a 3-D elastic half-space produces a log–log potency-area scaling with a slope of 3/2 for large earthquakes and a slope of 1 for small events. Their model realization with uncorrelated random property variation along the fault leads to a widening of the potency-area relation especially for weak seismicity. Ben-Zion & Zhu (2002) examined the potency-magnitude scaling of small to moderate earthquakes in southern California recorded by deep borehole and broadband instruments. The observations show a change from a slope of about 1 for earthquakes with local magnitude $M_L < 3.5$ to a slope of about 3/2 for earthquakes with $M_L > 5.5$. The results may be explained in terms of a transition from a limiting scaling $P_0 \propto S$ for small events propagating in a fractal-like stress field (Fisher *et al*. 1997) to a limiting scaling $P_0 \propto S^{3/2}$ for crack-like large events (Kanamori & Anderson 1975).

In the following we analyse the scaling between simulated values of earthquake potency and rupture area generated by our damage rheology model in a prescribed narrow fault zone in the regional lithospheric model of Fig. 5. A brittle failure at any fault location may lead to rupture propagation within the considered narrow fault zone. The damage evolution outside the prescribed fault zone is suppressed in these simulations. The calculations employ a quasi-dynamic procedure associated with a reduction (grey zone in Fig. 2) of the critical value of the damage variable at all elements of the model during the rupture process to a dynamic level α_d (Ben-Zion & Lyakhovsky 2006):

$$\alpha_d = \alpha_c - \sqrt{\tau_r \frac{d\alpha}{dt}}, \tag{21}$$

where τ_r is a material property controlling the weakening during the rupture propagation. This quasi-dynamic correction to the critical value of the damage variable is schematically shown in Fig. 2 as a grey zone. The damage failure threshold reverts everywhere to the static value α_c, defined by conditions (6) and (7), when the rupture stops propagating. The potency tensor of the simulated events is calculated using (19), where the integration covers all the elements in which damage achieved critical value during the seismic event. The scalar potency of the simulated earthquake is then calculated as:

$$P_0 = \sqrt{2 P_{ij} P_{ij}}. \tag{22}$$

The equivalent area S_e of the isometric tetrahedral grid element, with side length a and volume V_e, is calculated using the geometrical relation:

$$S_e = \frac{\sqrt{3}}{4} a^2 \approx 1.8 \cdot V_e^{2/3}. \tag{23}$$

Figs 7–9 give detailed results of model simulations implementing the stress-drop procedure discussed in Section 3 and boundary conditions discussed in Section 4 for various sets of rheological parameters. The results are in good agreement with the observations

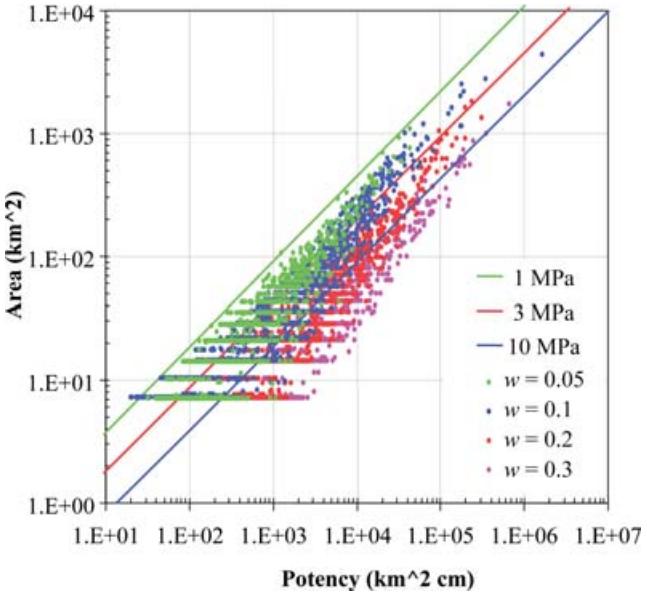

Figure 7. Simulated potency-area results for different values of the weight factor w. The other damage and loading parameters are $C_1 = 10^{-10}$ s^{-1}, $C_2 = 0.05$, $R = 0.3$ and $St = 10^5$ MPa. The lines are calculated with the theoretical relation of Kanamori & Anderson (1975).

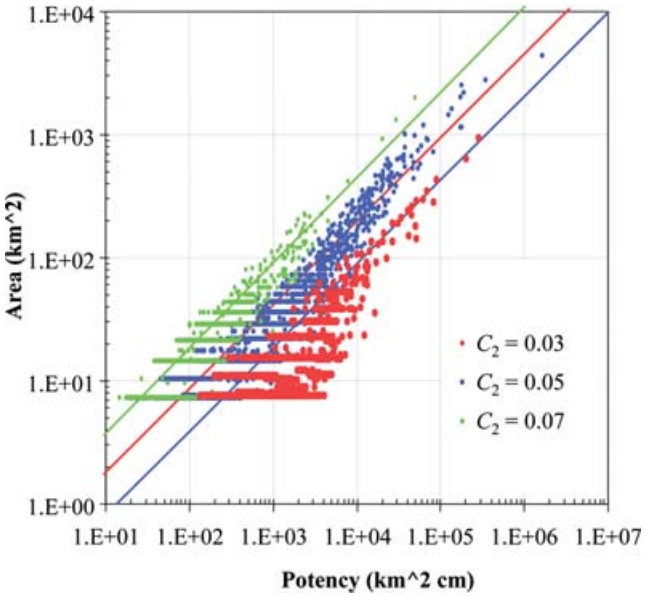

Figure 8. Simulated potency-area results for the model with different healing rate parameter C_2. The other model parameters are $w = 0.1$, $C_1 = 10^{-10}$ s^{-1}, $R = 0.3$ and $St = 10^5$ MPa.

of Kanamori & Anderson (1975) and Wells & Coppersmith (1994), and the simulations of Ben-Zion & Rice (1993) and Hillers *et al*. (2007) for moderate and large events. Points with the same colour represent earthquakes simulated with a fixed set of model parameters. Such points generally follow the lines calculated using (20) for $\Delta\sigma = 1$, 3 and 10 MPa; however, for some cases they fall outside the region bounded by those lines. The potency-area scaling relation can be shifted to larger or smaller values of the stress drop as a function of the damage parameters.

One of the key parameters controlling the local stress drop is the dynamic strain invariant ratio ξ_d, calculated using the weight

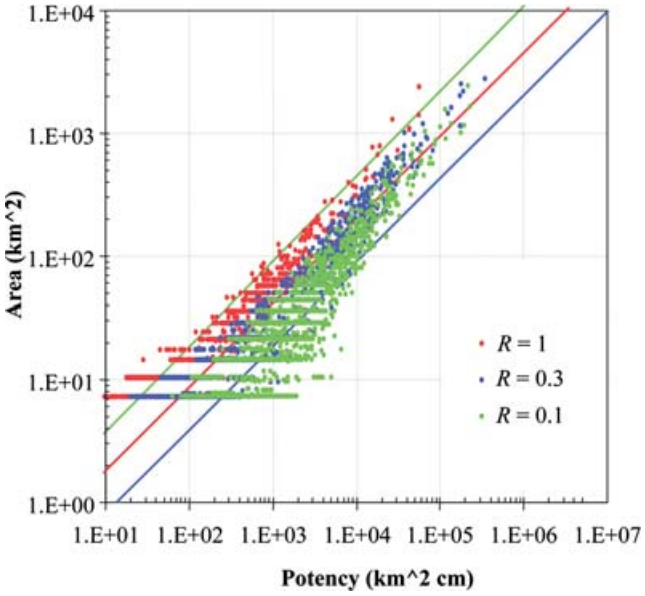

Figure 9. Simulated potency-area results for the model with different *R*-value. The other model parameters are $w = 0.1$, $C_1 = 10^{-10}$ s^{-1}, $C_2 = 0.05$, and $St = 10^5$ MPa.

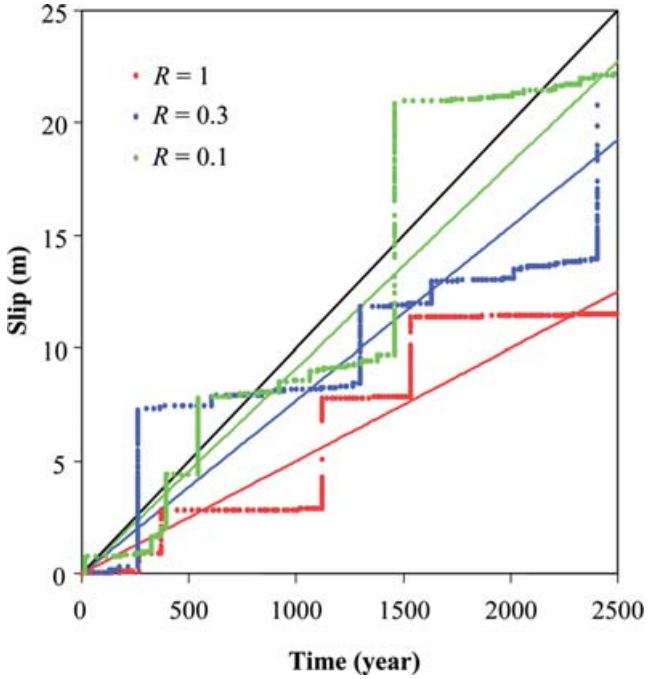

Figure 10. Simulated seismic slip versus time for models with different *R*-values. The black line gives the total slip associated with the remote motion. The coloured lines give the expected seismic slip based the seismic coupling coefficient $\chi = 1/(1 + R)$.

factor (10) and related to the effective residual or dynamic friction (Fig. 4). Small *w*-values correspond to large dynamic friction and relatively small stress drop. Reduced dynamic friction for larger *w*-values leads to a higher stress drop, expressed by a shifting of the potency-area scaling to the right. This is confirmed by a series of simulations with $w = 0.05$, 0.1, 0.2 and 0.3 (grey region in Fig. 4) and all the other model parameters the same (Fig. 7). The dynamic coefficient of friction (Fig. 4) is predicted to decrease only slightly with a change of the weight factor from 0.05 to 0.1. Accordingly, the potency-area scaling results for such cases (green and blue dots in Fig. 7) remain about the same, with only a small shift to the right for $w = 0.1$. The shift in the scaling results is much more significant for larger *w*-values (red and pink dots in Fig. 7), corresponding to a reduction of the dynamic friction up to 10 per cent for $w = 0.3$. The upper limit ($w = 1$, not shown here) with zero dynamic friction corresponds to a full local stress drop leaving only the volumetric component. This simplified stress-drop algorithm, adopted in our previous model realizations (Ben-Zion *et al*. 1999; Lyakhovsky *et al*. 2001a; Ben-Zion & Lyakhovsky 2002, 2006), underestimates the area of seismic events with a given potency. The simulations of Fig. 7 demonstrate that the potency-area scaling of the simulated events is sensitive to the weight factor. With fixed values of other model parameters, discussed further below, $w = 0.1$ produces potency-area scaling and stress drops compatible with the theoretical and observational results of Kanamori & Anderson (1975), Ben-Zion & Rice (1993), Wells & Coppersmith (1994) and Hillers *et al*. (2007).

The potency-area scaling is affected by the rheological parameters controlling the rate of damage healing and seismic coupling expressed through the *R*-value. The sensitivity to other model parameters controlling the onset of damage, kinetic of damage accumulation and dynamic weakening is very weak and is not shown. Following the propagation and arrest of brittle instabilities, the strength of a ruptured fault zone begins to recover with time (Fig. 1). The continuing load produced by the far field motion leads at some stage to a reversal of the damage kinetics from healing to weakening, and evolution towards the next seismic event which may rupture a stronger or weaker fault zone. The rate of damage healing directly affects the local stress drops during events, and hence shifts the potency-area scaling (Fig. 8). In the case of less efficient healing and weak fault zone (green dots in Fig. 8) the scaling relation follows the line corresponding to $\Delta\sigma = 1$ MPa. In contrast, the scaling relation for efficient healing (red dots in Fig. 8) and strong fault zone follow the line corresponding to $\Delta\sigma = 10$ MPa.

The stress drop is also reduced in fault zones with low seismic coupling χ given by eq. (5) or high *R*-values (Fig. 9). Enhanced accumulation of aseismic strain significantly reduces the seismic component of deformation and leads to smaller stress drops. The simulated scaling is shifted to the left (lower stress drop) for *R* changing from 0.1 (green dots in Fig. 9) to 1 (red dots in Fig. 9). Using the synthetic seismic catalogue, the average seismic slip may be calculated by multiplying the earthquake potency with the 100 km length of the fault zone and 20 km depth of the seismogenic zone. The coloured dots in Fig. 10 show the calculated seismic slip during 2500 yr of model runs with different *R*-values, while the coloured lines give the expected seismic slip calculated using eq. (5). The black line corresponds to the total slip associated with the imposed remote plate motion of 10 mm yr^{-1}. Every model run produces long-term oscillations between undershoot and overshoot responses associated with seismic quiescence and clustered seismic activity (Ben-Zion *et al*. 1999). In the long periods of low seismic activity, the model accumulates slip deficit. In the short periods of high clustered activity, the simulated seismic slip becomes larger than the predicted seismic slip, and sometimes also larger than the remote plate motion. However, the average seismic slip over thousands of years including many large earthquake cycles, calculated using the simulated values of earthquake potency, fits well the expected seismic slip calculated with the equation of the seismic coupling (5) predicted by the analytical results of Ben-Zion & Lyakhovsky (2006).

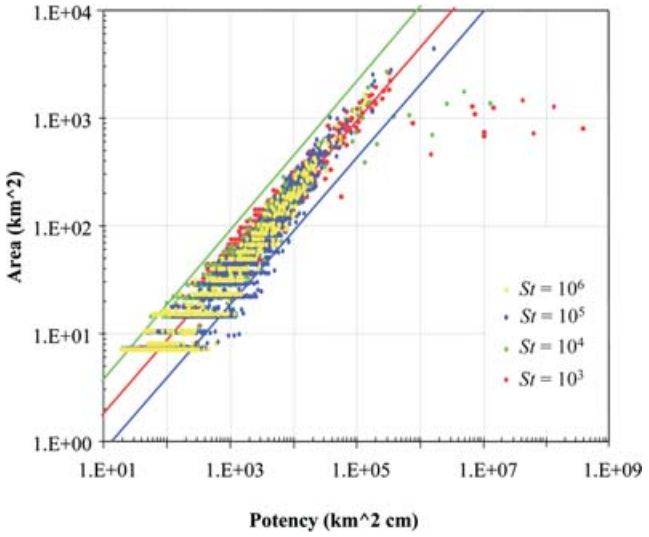

Figure 11. Simulated potency-area results for models with different stiffness St of the virtual boundary springs. The other model parameters are $w = 0.1$, $C_1 = 10^{-10}$ s^{-1}, $C_2 = 0.05$ and $R = 0.3$.

The area-potency relation for the simulated earthquakes may depend on the model boundary conditions, especially for events reaching close to the boundaries. Fig. 11 demonstrates the effects of the stiffness of the virtual springs used to implement the boundary conditions. Most of the simulated events in models with stiffness values in the range $St = 10^3 - 10^6$ MPa (coloured dots in Fig. 11) have very similar potency-area values. However, some events in the models with $St = 10^3$ MPa (red dots) and $St = 10^4$ MPa (green dots) have potency values several orders of magnitude larger then those predicted by eq. (20). System-size events, with rupture areas crossing the model boundaries, may produce significant boundary displacement if the stiffness of the virtual springs is relatively low. In such cases the slip is extended 'virtually' outside the simulated volume, but the model calculates only the area located inside the simulated domain. Therefore, the areas of these events are underestimated and the area-potency relation falls far from the expected relation. This effect disappears when the stiffness of the virtual springs increases to $St = 10^5$ MPa (blue dots) or $St = 10^6$ MPa (yellow dots).

6 DISCUSSION

We use a 3-D rheologically layered model of the lithosphere incorporating a thermodynamically based continuum rheology to study scaling relations of earthquakes and partition of elastic strain energy between seismic and aseismic components. Previous works have shown that the damage rheology model accounts for fundamental aspects of brittle rock deformation including subcritical microcrack growth from early stages of the loading, material degradation, and macroscopic brittle failure. In our previous studies of seismicity patterns we adopted the simplifying assumption that during brittle instabilities the local deviatoric stress drops to zero. This leads to an underestimation of the area of seismic events with a given potency. In this work, we develop a new mathematical formulation for calculating the local stress drop in failed zone where the damage achieved a critical value. The new algorithm utilizes the Drucker–Prager elasto-plastic behaviour for failed elements. The parameters of the yielding function are connected with dynamic friction of simpler models with planar faults.

A parameter-space study of the damage rheology parameters for a model with a single strike-slip fault (Fig. 5) demonstrates a good agreement between the scaling of rupture area and seismic potency values in simulated events and the theoretical relation of Kanamori & Anderson (1975). Most of the events (blue dots in Figs 7–9), simulated using model parameters $w = 0.1$, $C_1 = 10^{-10}$ s^{-1}, $C_2 = 0.05$, $R = 0.3$, fall within the area bounded by the green and blue lines corresponding to stress drops of 1 and 10 MPa. The results generally align with the red line for $\Delta\sigma = 3$ MPa calculated using the log–log scaling relation (20) with a slope of 2/3. The slope of the potency-area scaling remains the same ($S \propto P_0^{2/3}$) for simulated earthquakes with different sets of model parameters, but the results shift to lines associated with other stress drop values depending on the model parameters. Similarly to the results of Ben-Zion & Rice (1993), the scaling for small events has a large scatter and is not well constrained. The weight factor w, introduced in (10) to define the dynamic strain invariant ratio ξ_d, is the key parameter controlling the stress drop during the simulated seismic event. With increase of the w-value from zero to one, the dynamic friction decreases (Fig. 4) and the stress drop values increase.

Model parameters governing the damage evolution and loading conditions also affect the stress drop values. The healing parameters, C_1, C_2, control the level of damage that remains after the long interseismic periods. An efficient healing process leads to fast material recovery or strong fault zones with low damage values. In such cases the onsets of new brittle instabilities occur at higher stresses. In contrast, cases with low healing rates produce weak fault zones that sustain repeated failures at lower stress values. The gradual accumulation of irreversible strain, following the onset of damage and preceding the brittle instability (eq. 4), releases partially the elastic stress and reduces the stress drops during seismic events. However, this process leads only to small shifts of the potency-area scaling to lower stress drop values. The partition between seismic and aseismic deformation components is governed by the damage parameter R, associated with the ratio of the timescale for damage increase and timescale for viscous relaxation. Results of 3-D simulations demonstrate (Fig. 10) that the simple analytical eq. (5) of Ben-Zion & Lyakhovsky (2006) provides reasonable estimates for the average long-term seismic slip of fault zones with different R values.

The numerical simulations employ a modification of the previously developed code based on the FLAC algorithm. Variable boundary forces applied to the model edges are proportional to the slip-deficit between the far-field motion and displacement of the boundary nodes. These conditions account for the evolution of elastic properties and plastic strain accumulation in the model region, in contrast to the constant velocity or constant stress conditions used in traditional numerical models. The modified boundary conditions account for stress accumulation and strain-rate decrease during the interseismic periods, when the fault is locked, as well as abrupt stress reduction at the model boundary during seismic events. The potency-area scaling for most simulated events is not sensitive to the stiffness of the virtual springs used in the implementation of the boundary conditions (Fig. 11). Virtual springs with stiffness above 10^5 MPa eliminate artefacts associated with large events that reach the model boundaries (Fig. 11). Finzi *et al*. (2006) obtained a good agreement between surface deformation associated with system-size events generated by our model with such stiffness of virtual springs, and analytical solutions and FEM numerical simulations with viscoelastic rheology (e.g. Savage & Prescott 1978; Johnson & Segall 2004). The developments discussed in this paper provide an improved framework for studying the evolution of fault zone structures and the related seismic and aseismic deformation fields.

ACKNOWLEDGMENTS

The studies were supported by grants of the Southern California Earthquake Center (based on NSF cooperative agreement EAR-8920136 and United States Geological Survey cooperative agreement 14-08-0001-A0899), the Israel Ministry of Infrastructures (25-17-004) and the US–Israel Binational Science Foundation, Jerusalem Israel (2004046). We thank Y. Hamiel for useful discussions. The paper benefited from constructive reviews of the editor Y. Ricard and two anonymous referees.

REFERENCES

Agnon, A. & Lyakhovsky, V., 1995. Damage distribution and localization during dyke intrusion, in *The Physics and Chemistry of Dykes,* pp. 65–78, eds Baer, G. & Heimann, A., Balkema, Rotterdam.

Ampuero, J.-P. & Dahlen, F.A., 2005. Ambiguity of the moment tensor, *Bull. seism. Soc. Am.,* **95,** 390–400, doi:10.1785/0120040103.

Bazant, Z.P. & L. Cedolin, 1991. *Stability of Structures. Elastic, Inelastic, Fracture and Damage Theories,* Oxford University Press, New York, 984 p.

Beer G. 1983. Finite element, boundary element and coupled analysis of unbounded problems in elastostatics, *Int. J. Numer. Methods Eng.,* **19,** 567–580.

Beer G & Watson, J.O., 1992. *Introduction to Finite Boundary Element Method for Engineers,* Wiley, NY.

Ben-Zion, Y., 1989. The response of two joined quarter spaces to SH line sources located at the material discontinuity interface, *Geophys.J. Int.,* **98,** 213–222.

Ben-Zion, Y., 1996. Stress, slip, and earthquakes in models of complex single-fault systems incorporating brittle and creep deformations, *J. geophys. Res.,* **101,** 5677–5706.

Ben-Zion, Y., 2001. A note on quantification of the earthquake source, *Seism. Res. Lett.,* **72,** 151–152.

Ben-Zion, Y., 2003. Appendix 2, key formulas in earthquake seismology, in *International Handbook of Earthquake and Engineering Seismology,* Part B, pp. 1857–1875, eds Lee, W.H.K., Kanamori, H., Jennings, P.C. & Kisslinger, C., Academic Press, Amsterdam.

Ben-Zion, Y. & Lyakhovsky, V., 2002. Accelerating seismic release and related aspects of seismicity patterns on earthquake faults, *Pure Appl. Geophys.,* **159,** 2385–2412.

Ben-Zion, Y. & Lyakhovsky, V., 2006. Analysis of aftershocks in a lithospheric model with seismogenic zone governed by damage rheology, *Geophys. J. Int.,* **165,** 197–210.

Ben-Zion, Y. & Rice, J.R., 1993. Earthquake failure sequences along a cellular fault zon in a three-dimensional elastic solid containing asperity and nonasperity regions, *J. geophys. Res.,* **98,** 14 109–14 131.

Ben-Zion, Y. & Zhu, L., 2002. Potency-magnitude scaling relations for southern California earthquakes with 1.0<ML<7.0, *Geophys. J. Int.,* **148,** F1–F5.

Ben-Zion, Y., Dahmen, K., Lyakhovsky, V., Ertas, D. & Agnon, A.,1999. Self-driven mode switching of earthquake activity on a fault system, *Earth Planet. Sci. Lett.,* **172,** 11–21.

Bercovici, D. and Ricard, Y., 2003. Energetics of a two-phase model of lithospheric damage, shear localization and plate boundary formation, *Geophys. J. Int.,* **152,** 581–596.

Bercovici, D., Ricard, Y. & Schubert, G., 2001. A two-phase model for compaction and damage, part 1: general Theory, *J. geophys. Res.,* **106,** 8887–8906.

Brady, B.H.G. & Wassyng, A.A., 1981. Coupled finite element-boundary element method of stress analysis, *Int. J Rock Mech. Min. Sci. Geomech. Abstr.,* **18,** 475–485.

Budiansky, B. & O'Connell, R.J., 1976. Elastic moduli of a cracked solid, *Int. J. Solids Struct.,* **12,** 81–97.

Carter, N.L. & Tsenn, M.C., 1987. Flow properties of continental lithosphere, *Tectonophysics,* **136,** 27–63.

Collins, I.F., 2005. The concept of stored plastic work or frozen elastic energy in soil mechnics, *Geotechnique,* **55,** 373–382.

Collins, I.F. & Houlsby, G.T., 1997. Application of thermomechanical principles to the modelling of geotechnical materials, *Proc.Roy. Soc. Lond. A*, **453,** 1964, 1975–2001.

Cundall, P.A., 1989. Numerical experiments on localization in frictional materials, *Ign. Arch.,* **59,** 148–159.

Cundall, P.A. & Board, M., 1988. A microcomputer program for modeling large-strain plasticity problems, in *Numerical methods in geomechanics, Proc. 6th Int. Conf. Numerical Methods in Geomechanics, Innsbruck,* pp. 2101–2108, ed. Swoboda, C., Balkema, Rotterdam.

deGroot, S.R. & Mazur, P., 1962. *Nonequilibrium Thermodynamics,* North-Holland Publishing Co., Amsterdam, 510 p.

Dieterich, J.H., 1978. Time-dependent friction and the mechanics of stick-slip, *Pure and Appl. Geophys.,* **116,** 790–805.

Dieterich, J.H., 1979. Modeling of rock friction 1. Experimental results and constitutive equations, *J. geophys. Res.,* **84,** 2161–2168.

Drucker, D.C., 1949. Some implications of work-hardening and ideal plasticity, *Quart. Appl. Math.,* **7,** 411–418.

Drucker, D.C. & Prager, W., 1952. Soil mechanics and plastic analysis or limit design, *Quarterly Appl. Math.,* **10,** 157–164.

Ekland, I. & Temam, R., 1976. *Convex Analysis and Variational Problems,* Elsevier, New York.

Finzi, Y., Hearn, E.H., Lyakhovsky, V. & Ben-Zion, Y., 2006. 3D viscoelastic damage rheology models of strike-slip fault systems and their associated surface deformation, Eos Trans. AGU, **87**(52), *Fall Meet. Suppl., Abstract* T21 C-0425.

Fisher, D.S., Dahmen, K., Ramanathan, S. & Ben-Zion, Y., 1997. Statistics of earthquakes in simple models of heterogeneous faults, *Phys. Rev. Lett.*, **78,** 4885–4888.

Hamiel, Y., Liu, Y., Lyakhovsky, V., Ben-Zion, Y. & Lockner, D., 2004. A visco-elastic damage model with applications to stable and unstable fracturing, *J. geophys. Int.,* **159,** 1–11.

Hamiel, Y., Lyakhovsky, V. & Agnon, A., 2005. Rock dilation, nonlinear deformation, and pore pressure change under shear. *Earth Planet. Sci. Lett.,* **237,** 577–589.

Hamiel, Y., Katz, O., Lyakhovsky, V., Reches, Z. & Fialko,Y., 2006. Stable and unstable damage evolution in rocks with implications to fracturing of granite, *Geophys. J. Int.,* **167,** 1005–1016.

Heaton, H.T. & Heaton, R.E., 1989. Static deformation from point forces and force couples located in welded elastic Poissonian half-spaces: implications for seismic moment tensors, *Bull. seism. Soc. Am.,* **79,** 813–841.

Hill, R., 1998. *The Mathematical Theory of Plasticity,* Oxford University Press, Oxford, 366 pp.

Hillers, G., Mai, P.M., Ben-Zion, Y. & Ampuero, J.-P., 2007. Statistical properties of seismicity along fault zones at different evolutionary stages, *Geophys. J. Int.,* **169,** 515–533.

Hirth, G. & Kohlstedt, D.L., 1996. Water in the oceanic upper mantle: implications for rheology, melt extraction and the evolution of the lithosphere, *Earth Planet. Sci. Lett.,* **144,** 93–108.

Hirth, G. & Kohlstedt, D.L., 2003. Rheology of the upper mantle and the mantle wedge: a view from the experimentalists, in the subduction factory, *Geophys. Monogr.,* Vol. 138, pp. 83–105, ed. Eiler, J., AGU, Washington DC.

Ilchev, A. & Lyakhovsky, V., 2001. Practical aspects of the hybridization of the boundary integral method with damage rheology modeling for the assimilation of seismic data, in *Dynamic Rock Mass Response to Mining, Rockbursts and Seismicity in Mines – RaSiM5,* pp. 421–426, eds van Aswegen, G., Durrheim, R.J. & Ortlepp, W.D., South African Institute of Mining and Metallurgy, Johannesburg, SA.

Jing, L. & Hudson, J.A., 2002. Numerical methods in rock mechanics, *Int. J. Rock Mech. & Mining Sci.,* **39,** 409–427.

Johnson, K.M. & Segall, P., 2004. Viscoelastic earthquake cycle models with deep stress-driven creep along the San Andreas fault system, *J. geophys. Res.,* **109,** doi:10.1029/2004JB003096.

Kachanov, L.M., 1986. *Introduction to Continuum Damage Mechanics,* Martinus Nijhoff Publishers, Dordrecht, 135 p.

Kanamori, H. & Anderson, D.L., 1975. Theoretical basis of some empirical relations in seismology. *Bull. seism.. Soc. Am.,* **65,** 1073–1095.

Kohlstedt, D.L., Evans, B. & Mackwell, S.J., 1995. Strength of the lithosphere: constraints imposed by laboratory experiments, *J. geophys. Res.,* **100,** 17 587–17 602.

Krajcinovic, D., 1996. *Damage Mechanics,* Elsevier, Amsterdam.

Linker, M.F. & Dieterich, J.H., 1992. Effects of variable normal stress on rock friction: observations and constitutive equations, *J. geophys. Res.,* **97,** 4923–4940.

Lyakhovsky, V. 2001. Scaling of fracture length and distributed damage, *Geophys. J. Int.,* **144,** 114–122.

Lyakhovsky, V. & Myasnikov, V.P., 1984. On the behavior of elastic cracked solid, *Phys. Solid Earth,* **10,** 71–75.

Lyakhovsky, V. & Myasnikov, V.P., 1985. On the behavior of visco-elastic cracked solid, *Phys. Solid Earth,* **4,** 28–35.

Lyakhovsky, V., Podladchikov, Y. & Poliakov, A., 1993. Rheological model of a fractured solid, *Tectonophysics,* **226,** 187–198.

Lyakhovsky, V., Ben-Zion, Y. & Agnon, A., 1997a. Distributed damage, faulting, and friction, *J. geophys. Res.,* **102,** 27 635–27 649.

Lyakhovsky, V., Reches, Z., Weinberger, R. & Scott, T.E., 1997b. Non-linear elastic behavior of damaged rocks, *Geophys. J. Int.,* **130,** 157–166.

Lyakhovsky, V., Ben-Zion, Y. & Agnon, A., 2001a. Earthquake cycle, faults, and seismicity patterns in rheologically layered lithosphere, *J. geophys. Res.,* **106,** 4103–4120.

Lyakhovsky V., Ilchev A. & Agnon A., 2001b. Modeling of damage and instabilities of rock mass by means of a non-linear rheological model, in *Dynamic rock mass response to mining, Rockbursts and Seismicity in Mines – RaSiM5,* pp. 413–420, eds van Aswegen, G., Durrheim, R.J. & Ortlepp, W.D., South African Institute of Mining and Metallurgy, Johannesburg, SA.

Lyakhovsky, V., Ben-Zion, Y. & Agnon, A., 2005. A viscoelastic damage rheology and rate- and state-dependent friction, *Geophys. J. Int.,* **161,** 179–190.

Malvern, L.E., 1969. *Introduction to the Mechanics of a Continuum Medium,* Prentice-Hall, Inc., New Jersey, 713 p.

Martyushev, L. & Seleznev, V., 2006. Maximum entropy production principle in physics, chemistry and biology, *Physics Reports,* **426,** 1–45.

Molnar, P. & Jones, C.H., 2004. A test of laboratory based rheological parameters of olivine from an analysis of late Cenozoic convective removal of mantle lithosphere beneath the Sierra Nevada, California, USA, *Geophys. J. Int.,* **156,** 555–564 doi:10.1111/j.1365-246X.2004.02138.x.

Mosolov, P.P. & Myasnikov, V.P., 1965. Variational methods in flow theory of visco-plastic media, *Appl. Math. and Mech.,* **29,** 468–492 (in Russian).

Mosolov, P.P. & Myasnikov, V.P., 1981. *Mechanics of Rigid Plastic Media,* Nauka, Moscow (in Russian).

Newman, W.I. & Phoenix, S.L., 2001. Time-dependent fiber bundles with local load sharing, *Phys. Rev. E.,* **63**, 021507.

Onsager, L., 1931. Reciprocal relations in irreversible processes, *Phys. Rev.,* **37,** 405–416.

Poliakov, A., Cundall, P., Podladchikov, Y. & Lyakhovsky, V., 1993. An explicit inertial method for the simulation of viscoelastic flow: an evaluation of elastic effects on diapiric flow in two- and three-layers model, in *Proc. NATO Advanced Study Institute on Dynamic Modeling and Flow in the Earth and Planets,* pp. 175–195, eds Runcorn, K.E. & Stone, D., Kluwer, Dordrecht.

Prager, W., 1959. *An Introduction to Plasticity,* Addison-Wesley, Amsterdam.

Prigogine, I., 1955. *Introduction to Thermodynamics of Irreversible Processes*. Springfield, Illinois.

Rabotnov, Y.N., 1988. *Mechanics of Deformable Solids,* Science, Moscow, 712 p.

Ricard, Y. & Bercovici, D., 2003.Two-phase damage theory and crustal rock failure: the theoretical "void" limit, and the prediction of experimental data, *Geophys. J. Int.,* **155,** 1057–1064.

Rice, J.R., 1980. The mechanics of earthquake rupture, in *Physics of the Earth's Interior,* pp. 555–649, eds Dziewonski, A.M. & Boschi, E., Italian Physical Society/North Holland, Amsterdam.

Rudnicki, J.W. & Rice, J.R., 1975. Conditions for the localization of deformation in pressure-sensitive, dilatant materials, *J. Mech. Phys. Solids,* **23,** 371–394.

Savage, J.C. & Prescott, W.H., 1978. Asthenosphere readjustment and the earthquake cycle, *J. geophys. Res.,* **83,** 3369–3376.

Schreyer, H.L. & Neilsen, M.K., 1996a. Analytical and numerical tests for loss of material stability, *Int. J. Numer. Methods Eng.,* **39,** 1721–1736.

Schreyer, H.L. & Neilsen, M.K., 1996b. Discontinuous bifurcation states for associated smooth plasticity and damage with isotropic elasticity, *Int. J. Solids Structures.,* **33,** 3239–3256.

Sedov, L.I., 1968. Variational methods of constructing models of continuous media, in *Irreversible Aspects of Continuum Mechanics,* pp. 17–40, Springer, Berlin.

Shcherbakov, R. & Turcotte, D.L., 2003. Damage and self-similarity in fracture. *Theor. Appl. Fracture Mech.,* **39,** 245–258.

Strehlau, J. & Meissner, R., 1987. Estimation of crustal velocities and shear stress from an extrapolation of experimental steady state flow data, in *The composition Structure, and Dynamics of the Lithosphere-Astenosphere System,* pp. 69–86, eds Fuchs, K. & Froidevaux, C., Geodynamics Series, AGU, Vol. 16, Washington, D.C.

Turcotte, D.L. & Schubert, G., 2002. *Geodynamics,* 2nd edn, John Wiley & Sons, New York.

Turcotte, D.L., Newman, W.I. & Shcherbakov, R., 2003. Micro and macroscopic models of rock fracture. *Geophys. J. Int.,* **152,** 718–728.

Washizu, K., 1982. *Variational Methods in Elasticity and Plasticity,* 3rd edn, 630 p. Pergamon Press Ltd., Oxford.

Weertman, J., 1978. Creep laws for the mantle of the Earth. *Philos. Trans. R. Soc. London A,* **288,** 9–26.

Weinberger, R., Reches, Z., Eidelman A. & Scott, T.E., 1994. Tensile properties of rocks in four-point beam tests under confining pressure, in *Rock Mechanics Models and Measurements Challenges from Industry,* pp. 435–442, eds Nelson, P. & Laubach, S.E., Balkema, Rotterdam.

Wells, D.L. & Coppersmith, K.J., 1994, New empirical relationships among magnitude, rupture length, rupture width, rupture area and surface displacement. *Bull. Seismol. Soc. Am.,* **84,** 974–1002.

Zeller, S.S. & Pollard, D.D., 1992. Boundary conditions for rock fracture analysis using boundary element method. *J. geophys. Res.* **97,** 1991–1997.

Ziegler, H., 1983. *An Introducton to Thermomechanics,* 2nd edn, 358 pp., Amsterdam, North-Holland Publishing Company

Zienkiewicz, O.C., Kelly, D.W. & Bettess, P. 1977. The coupling of the finite element method and boundary solution procedures. *Int. J. Numer. Methods Eng*., **11,** 355–375.

Zöller, G., Hainzl, S., Ben-Zion, Y. & Holschneider, M., 2006. Earthquake activity related to seismic cycles in a model for a heterogeneous strike-slip fault, *Tectonophysics,* **423,** 137–145.